A Study of the Wavenumber Spectra of Short Water Waves in the Ocean

PAUL A. HWANG

Oceanography Division, Naval Research Laboratory, Stennis Space Center, Mississippi

SERHAD ATAKTURK

Department of Atmospheric Science, University of Washington, Seattle, Washington

MARK A. SLETTEN AND DENNIS B. TRIZNA

Remote Sensing Division, Naval Research Laboratory, Washington, D.C.

(Manuscript received 18 May 1995, in final form 11 December 1995)

ABSTRACT

Spatial measurements of capillary–gravity waves in the ocean were obtained using a scanning slope sensor mounted on a free-drifting buoy intended to minimize the flow disturbance. The data provide direct calculation of the wavenumber spectra of surface curvature in the capillary–gravity wave range. The results indicate that 1) a pronounced peak at the wavenumber $k = 9$ rad cm^{-1} is evident in the curvature spectra for wind speeds below 6 m s^{-1}; 2) the slopes of the curvature spectra are 1 and -1 on the two sides of the spectral peak; 3) the spectral density and mean-square roughness properties increase linearly with wind speed; and 4) these observations suggest a spectral function of the form $\chi(k) = Au_*c^{-2}c_mk_mk^{-4}$, which is proportional to u_*k^{-3} in the short gravity wave region and u_*k^{-5} in the capillary wave region, where u_* is the wind friction velocity, c_m the minimum phase velocity of surface waves, and k_m the corresponding wavenumber.

Capillary–gravity wave wavenumber spectra obtained from the ocean and from laboratory studies are compared. It is found that significant differences in many important features of short-wave properties exist in the datasets from these two different environments. A possible reason for the observed differences is attributed to the fluctuation component of the wind field, which is typically a significant fraction of the mean wind speed in the open ocean but much smaller in the laboratory. The steady wind in the laboratory produces a surface boundary condition very different from that in the field. This is reflected in the observation that a spectral *gap* in the vicinity of the minimum phase velocity (an indication of wave blockage by steady surface drift current) was found in the laboratory measurements but not in the field data. As a consequence, the small-scale structures observed in the laboratory and in the field are significantly different.

1. Introduction

The study of wind-generated capillary–gravity (CG) waves is motivated by our interest in air–sea interactions and microwave remote sensing of the ocean surface. In the case of air–sea interactions, the momentum exchange from air to water results in the inception of CG waves, which grow into longer gravity waves. The presence of surface waves subsequently modifies the roughness and the boundary condition on the water surface and, thus, further enhances the exchange of momentum between air and water. In the case of radar remote sensing, water waves serve as roughness elements on the ocean surface to cause scattering of radar waves. For moderate incidence angles, Bragg scattering has been considered a primary mechanism of radar backscatter (e.g., Wright 1966, 1968); for low grazing angles, steep curvature features on the water surface and radar sea spike events are found to be closely correlated (Trizna et al. 1993; Wetzel 1993).

For the X-band and K-band radars, the Bragg wavelength is on the order of between a few millimeters and a few centimeters in the CG region. Since the possibility of using radar as a wave spectrometer was proposed over four decades ago (e.g., Crombie 1955), attempts have been made to derive the spectra of CG waves. However, reports on the wavenumber spectra derived from microwave radars from different investigators and/or different experiments have been found to be rather inconsistent. In many cases, these reported spectra disagree in terms of both the spectral level and the spectral slope, two of the most important properties characterizing the spectral function (see, for example, the comparisons and discussions in Lawner and Moore 1984). Such discrepancies may be attributed to the fact

Corresponding author address: Dr. Paul A. Hwang, Naval Research Laboratory, Code 7332, Stennis Space Center, Bay St. Louis, MS 39529-5004.

that many mechanisms contribute to the backscatter of radar waves from the ocean surface. In addition to the well-studied mechanisms of surface tilting and Bragg resonance, contributions from breaking waves, wedges, and jumps are probably much more important than previously realized (e.g., Donelan and Pierson 1987; Phillips 1988; Trizna et al. 1993; Wetzel 1993). None of these non-Bragg processes can be considered well understood and quantifiable at this stage. It is noted that the present short-wave spectral models used for evaluation of the Bragg contribution are based mostly on laboratory measurements of high-frequency spectra, and model results differ considerably from measurements derived from the ocean (Shemdin and Hwang 1988). Without reliable knowledge of the wave characteristics in the short-wave region, it is difficult to evaluate the insufficiency of the Bragg scattering mechanism, and many schemes proposed to make modifications beyond Bragg scattering can only be considered as speculative.

As a different approach for determining the short-wave spectra, many theoretical and semiempirical studies have been conducted to investigate the spectral properties in the saturation region, loosely defined as the band of wave components with frequencies higher than 3 times the spectral peak frequency, or wavelengths 10 times shorter than the dominant wavelength. Some of the theories are limited to the range before surface tension effects set in (e.g., Phillips 1985; Banner 1990), and some extend to the region where viscous damping is significant (e.g., Donelan and Pierson 1987). As these theories may vary in the choice of mechanisms governing the spectral or action density balance (wind forcing, dissipation, and nonlinear wave–wave interactions are considered the three most important ones), the final results invariably hinge on the formulation of these source/sink functions. For example, Phillips (1985) suggests that all three source/sink terms are important in the saturation range. Through a detailed discussion, he reaches the conclusion that the two-dimensional spectral function $\Psi(\boldsymbol{k})$ of short gravity waves increases linearly with the wind friction velocity u_* and the spectral slope is -3.5. This can be expressed as $\Psi(\boldsymbol{k}) \sim u_* k^{-3.5}$ or, equivalently, for the omnidimensional spectrum $\chi(k) \sim u_* k^{-2.5}$, where k is the wavenumber. In addition, the dissipation function is shown to be a cubic function of the degree of saturation defined as $B(\boldsymbol{k}) = k^4\Psi(\boldsymbol{k})$, which is closely related to the curvature spectrum. In contrast, Donelan and Pierson (1987) argue for a local balance in the short-wave region and neglect the wave–wave interactions term in the formulation. Based on field observations of gravity wave spectra and backscatter in the K_u band, the breaking dissipation is formulated as a smooth function that asymptotically approaches $3.58 \times 10^9 B^5$ in the gravity wave region and $9.95 \times 10^2 B^{1.15}$ in the short capillary–gravity wave region. Donelan and Pierson also suggest that the proper reference wind speed for each wave component should be the velocity at an elevation scaled to the wave component's wavelength. In the absence of knowledge of the detailed structure of the wind field above an undulating random surface, a logarithmic profile is extended all the way to the water surface. The resulting spectra at high wavenumbers are shown to be very sensitive to the water temperature as a result of viscous damping. The variation of spectral slope in the CG region is somewhat complicated, and wind speed dependence of the spectral level in the CG range cannot be expressed in simple functions.

Because of the difficulties in resolving the short-wave spectral function either by remote sensing techniques or through theoretical development, direct wave measurements in the field and laboratory remain one of the most important resources for understanding the characteristics of short waves. Due to the large volume of published literature on this subject, however, only a portion related to field measurements of short waves in the CG range is referenced here. One of the earliest studies of the statistical properties of short waves is that of Cox and Munk (1954), who established the linear relationship between the mean square slope and the wind speed. Subsequent efforts have been devoted mainly to resolving the spectral composition of short waves. The most fruitful instrument for field measurements of CG wave spectra is probably the laser slope gauge (Palm et al. 1977; Hughes et al. 1977; Hughes and Grant 1978; Hughes and Gower 1983; Tang and Shemdin 1983; Hwang and Shemdin 1988; Shemdin and Hwang 1988). The laser slope gauge measures the refraction of a laser beam passing through the air–water interface. From Snell's law, the surface slope can be derived from the angle of refraction. Because only a single fixed beam was used in the past, time series and frequency spectra were obtained. Attempts to convert these frequency spectra to the wavenumber domain have been controversial due to the large Doppler frequency shift in CG waves on the ocean surface. Although the kinematics of the Doppler effect is well known, the conversion procedure requires a priori knowledge of the directional distribution. The dynamic processes of blockage and wave breaking, both of which are clearly irreversible, further introduce considerable difficulties for carrying out the frequency-to-wavenumber conversion.

To mitigate the difficulty of interpreting the frequency measurements, spatial scanning using a laser beam appears to be a logical solution. The approach is favored for field measurements because the operating principle is simply the optical refraction of a single beam, a principle found to be robust and reliable in the past. The first two-dimensional scanning slope sensor was developed by researchers at TRW for mounting on the bow of a ship to obtain spatial measurements of CG waves in the ocean (Lee et al. 1992). Wavenumber spectra in the wavelength range from 2.5 to 9.5 cm are

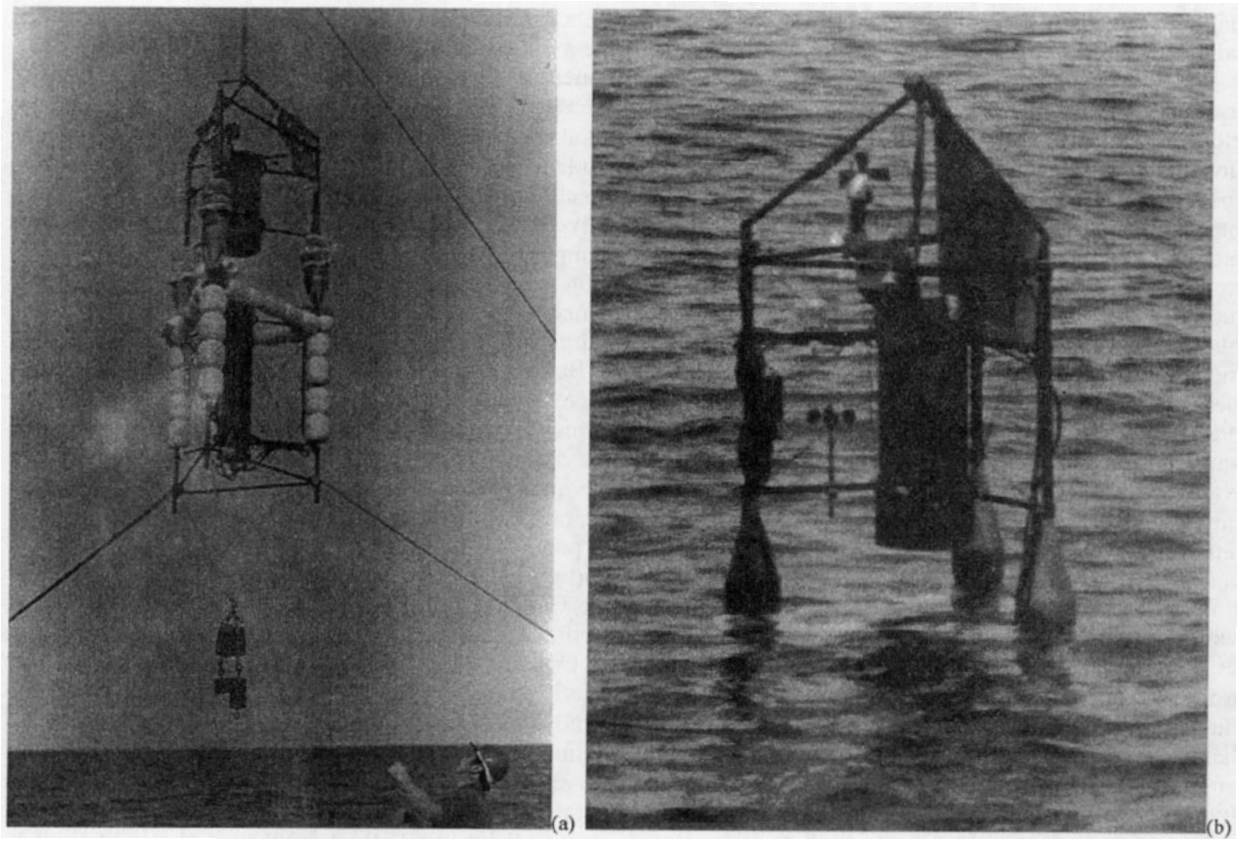

FIG. 1. (a) A picture of the scanning slope sensor buoy system in the process of deploying into the ocean, showing the open-frame design and the subsurface flotation arrangement. (b) The buoy released in free drift to obtain optical measurements of capillary–gravity waves on the ocean surface.

presented. The spectral shape is shown to be somewhat steeper than k^{-4}. Martinsen and Bock (1992) discuss the development of a scanning slope sensor mounted on a pontoon, and Hara et al. (1994) present data collected from this system moored near a pier at the Woods Hole facilities. The measurement location was approximately 30 m offshore with a mean depth of 2 m. Wavenumber spectra at three wind friction velocities, 5.5, 9.6, and 22 cm s^{-1} are given.

In this paper, wavenumber spectra obtained from a scanning slope sensor system mounted on a free-drifting buoy are presented. A description of the instrumentation system and field experiment is given in section 2. The data processing procedure is described in section 3, with emphasis on the treatment of surface slope data obtained from a moving platform and the compensation of ambient light contamination to the optical signals. A discussion of the wavenumber spectra of CG waves ($1 < k < 16$ rad cm^{-1}) from the ocean is presented in section 4. The derivation of the dimensionless spectral coefficient is given in section 5, along with a discussion of some implications on the generation mechanisms of CG waves and a comparison of field results with laboratory measurements of short wind waves. A summary of the paper is provided in section 6.

2. Instrumentation and field experiment

Figure 1a shows the scanning slope sensor (SSS) buoy suspended by a crane prior to deployment in the ocean. The buoy structure is constructed from light triangular frames made of aluminum tubes (see appendix A). Subsurface floats are used to provide the wave-following capability without introducing significant surface disturbance. The optical scanning and receiving units are secured at the center of the triangular structure. Figure 1b shows the deployed buoy in free drift. The free-drifting mode of operation is considered a key factor to the reduction of flow disturbance. Because there have been serious criticisms regarding the possible contamination of short-wave properties in the sensing region by structure-generated disturbances (e.g., Dobson 1985), we have carefully examined many enlarged pictures and video images similar to that shown in Fig. 1b, in an attempt to detect the presence of ring waves or wakes around the structural members piercing through the air–water interface. This type of

disturbance is frequently found in the vicinity of fixed structures or around an actively moving platform, but it has not been detected in the case of the surface-following SSS buoy in free drift. It is reasonable to conclude that, by reducing the relative velocity between the surface current and the structural members piercing through the water surface, we have achieved a significant improvement in reducing local wave generation by the buoy members and flow distortion to the sensing region.

The key instrument for CG wave measurements is the scanning slope sensor. In the current design, a laser beam scans a two-dimensional pattern of eight linear segments spaced 0.5 cm apart. Each linear segment 10 cm in length is sampled at 50 positions with an equal spacing of 0.2 cm. The duration to sample the 50 positions is 2.5 ms, and the mechanical flyback time of the scanning mirror facets to generate two consecutive scan lines is 4.3 ms. The excess time is used to sample the other instruments, which are described in the next paragraph. In this paper, the one-dimensional wavenumber spectra using the central 32 points are presented. Each linear scan is treated as an individual observation. The effective spatial coverage is 6.2 cm, and the shortest wavelength resolvable is 0.4 cm. The optical scanning speed is 40 m s^{-1} (= 10 cm distance in 2.5 ms), much faster than the phase speed of the CG waves being measured, and the surface can be considered "frozen." The processing of two-dimensional wavenumber (k_x, k_y) and three-dimensional wavenumber–frequency (k_x, k_y, ω) spectra is in process. For the eight-line two-dimensional coverage, the frame repetition rate is slightly higher than 30 frames per second. This relatively low repetition rate is due to the speed of the data acquisition hardware (20 000 samples per second per slope component) available at the time of system fabrication (September 1991). The results from the two- and three-dimensional data analysis will be presented later. Details regarding the operation principles and the equations related to the derivation of surface slope from the refraction of a laser beam have been fully discussed in the literature on laser slope gauges cited above and will not be repeated here. A detailed description of a similar scanning slope sensor developed for laboratory use is presented elsewhere (Hwang 1992; Hwang et al. 1993).

In addition to the scanning slope sensor, the buoy also carries two wind sensors, two thermometers to measure the temperatures of air and water, two accelerometers to monitor the long waves, two pressure sensors to measure the instantaneous water elevation above the scanning unit, and a compass to monitor the orientation of the buoy structure and wind direction. The surface wind stress, or equivalently, the wind friction velocity, can be calculated from wind speed at a given elevation, humidity, and temperatures of air and water near the air–water interface. For low wind conditions, as we have encountered in this experiment, the stability correction (from wind speed, humidity, and temperature information) and the consideration of molecular transport near the air–water interfacial sublayer are especially important. The LKB algorithm (Liu et al. 1979) is used for the calculation of wind friction velocity from buoy measurements. The humidity data is obtained from the meteorological dataset collected on board of the research vessel by J. Edson (Woods Hole Oceanographic Institute).

The wind direction output from the wind sensor is used to monitor the deviation of the buoy orientation with respect to the instantaneous wind direction. All the data are recorded simultaneously on the computer carried inside the scanning unit. The capacity of the computer hard disk is 300 megabytes, capable of storing two and one-half hours of continuous data. All the data collections are performed with the buoy in free drift to minimize the relative velocity between the moving water and the structural members piercing through the air–water interface. To further reduce the flow disturbance to the sensing region, a wind vane is used to orient the buoy such that an open face of the triangular structure is facing upwind. The wind vane also aligns the scanning direction to be along the wind direction. The whole system is powered by a rechargeable battery that outlasts the capacity of the hard disk. More details of the mechanical system and the technical specifications of sensors mounted on the buoy are provided in appendix A.

The field experiment is a part of the Office of Naval Research High Resolution Accelerated Research Initiative (HiRes ARI). It was organized to study the submesoscale features near the Gulf Stream boundaries using remote sensing techniques (spaceborne, airborne, shipborne, and land-based radars) and in situ measurements of relevant atmospheric and oceanographic parameters. During the two weeks from 10 June to 26 June 1993, the scanning slope sensor buoy was deployed to measure the short-wave properties in the ocean. A total of 18 datasets were collected, and a subset of six runs under favorable ambient light conditions was selected for presentation in this article. Figure 2 shows a map of the area and the locations of the buoy during the six selected runs. The region is close to the northern boundary of the Gulf Stream (depicted as a dashed curve in the lower right corner of the figure), with very active convergence zones in air and water. The general circulation pattern in the area is very complicated, as seen in Fig. 2 from the average buoy trajectories of the six deployments (for each sequence, the deployment location is marked with "○" and the retrieval location is marked with "+"). A summary of the background information of the six cases, arranged in order of increasing mean-square curvature, is given in Table 1. Slick bands on the water surface were frequently observed at low wind conditions. In particular, for both cases 1810 and 2422 (Table 1), scattered slick bands were visible in the deployment region. Interest-

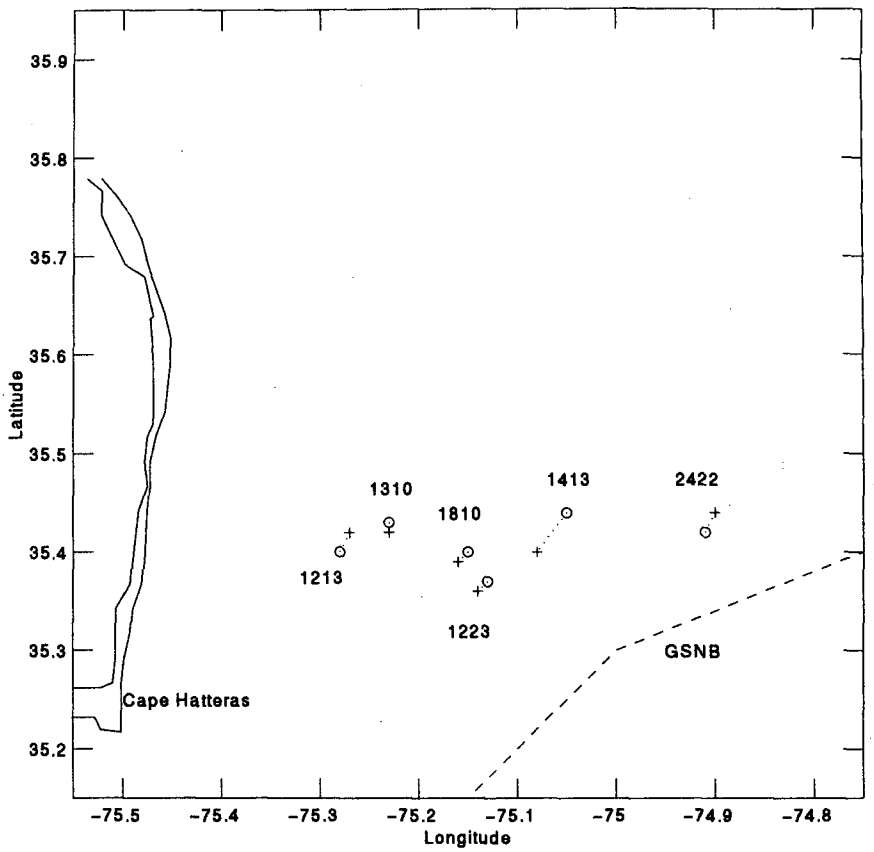

FIG. 2. Area map showing the locations of buoy deployment (○) and retrieval (+) for the six experimental cases presented in this article.

ingly, the spectral characteristics of these two cases are distinctly different (to be further discussed in the next section). Because we do not have a reliable way of identifying slick encounters from the collected data suite at this stage, the spectral computation is performed over the full data length indicated in Table 1. These spectra are considered to be representative of the average spectra in a biologically active surface environment. Also, as indicated in the column of wind fluctuation (σ_U), it is emphasized that a truly steady condition in the field is very rare. It will be shown later (§5c) that unsteadiness as a natural parameter may play

TABLE 1. Experimental conditions arranged in the order of ascending surface roughness measured by the mean-square curvature. Key to symbols: Case number convention, identified with four digits, *ddhh*, where *dd* represents the date in June 1993 and *hh* represents the hour (UTC) when the buoy was deployed (subtract 4 from UTC to get local time); Length, total data length in seconds; s_{11}, the mean square curvature; $U_{1.33}$, the wind velocity at 1.33 m above the mean water level (relative to the moving water surface) measured by the wind sensor on the buoy; σ_U, the root-mean-square wind speed fluctuation; T_w, the water temperature; T_a, the air temperature; Ambient, the ambient light intensity normalized by the signal intensity; C_{avg}, the average current derived from the coordinates of buoy deployment and retrieval; U_{10}, the equivalent neutral wind speed at 10 m high; u_*, the surface wind friction velocity; and z_0, the dynamic roughness height. The last three quantities are derived using the LKB algorithm (Liu et al. 1979). The cgs units are used throughout this article, unless specified otherwise.

Case	Length (s)	s_{11} (cm^{-2})	$U_{1.33}$ ($m\ s^{-1}$)	σ_U ($m\ s^{-1}$)	T_w (°C)	T_a (°C)	Ambient (*N/S*)	U_{10} ($m\ s^{-1}$)	u_* ($cm\ s^{-1}$)	z_0 (mm)	$\frac{U_{10}}{U_{1.33}}$	C_{avg} ($m\ s^{-1}$)
1213	2000	0.0050	0.69	0.262	23.21	23.28	0.76	0.84	2.9	0.063	1.21	0.16
1810	1000	0.0084	1.10	0.165	23.27	23.58	0.60	1.33	4.4	0.039	1.21	0.21
2422	5200	0.125	1.08	0.536	26.27	24.20	0.29	1.31	4.7	0.046	1.21	0.48
1413	4390	0.184	1.74	0.440	20.75	21.17	0.45	2.08	6.8	0.031	1.20	0.31
1310	3000	0.308	2.94	0.619	22.83	22.76	0.42	3.54	11.9	0.054	1.20	0.16
1223	2190	0.467	4.69	0.397	23.52	22.28	0.15	5.72	20.5	0.121	1.22	0.40

an important role in the shaping of the short-wave characteristics in the ocean.

The collocated and simultaneously measured data (two slope components, two pressure sensors, two accelerometers, two wind sensors, two temperature sensors, one compass, and one wind direction output) are stored in short segments approximately 10-s long (the data length is dynamically adjusted to use the maximum free memory on the computer, which may vary with different configurations). For each data segment of approximately 10 s, 1800 spectra are computed, resulting in 180 000 to 936 000 spectral realizations for each case presented in this article. Further discussion of the data processing procedure is given in the next section.

3. Data processing

a. Buoy motion and trend removal

Because each scan of the slope data covers a 6.2-cm distance, trend removal is necessary to reduce spectral leakage from tilting due to longer waves and the motion of the buoy platform. A prewhitening procedure described in Mitsuyasu (1977) and Banner et al. (1989) is used. The data trend is removed by taking the spatial derivative of the slope space series. The results are the space series of the longitudinal curvature component η_{11}, where η is the surface displacement, the subscript denotes differentiation, and 1 is in the scanning direction, which is also the dominant wind direction based on the instrument alignment. [Here we have identified the second derivative of the surface displacement with curvature. The mean-square slope in the present dataset is on the order of 10^{-2}, as discussed in section 5c. The additional term $(1 + \eta_1^2)^{3/2}$ in the full expression of curvature $\eta_{11}(1 + \eta_1^2)^{-3/2}$ introduces a correction of less than 1%, which is considered negligible.] An example of the results using this data processing procedure is shown in Fig. 3. A simulated slope signal composed of 40 short-wave components, each with random phase and random amplitude, is riding on a background tilting surface, simulated by a sinusoidal wave with a 25° amplitude, a 1-m wavelength, and a random phase (Fig. 3a). The perturbation due to the slow surface undulation can be successfully removed by the finite difference procedure, shown as circles in Fig. 3b. For comparison, the "true" curvature with no background tilting is given as dashed lines. For higher levels of slope signal, the two curvature series are essentially identical; as the signal level reduces, the difference in the two spatial series increases. Figure 3c plots the ratio s'/s versus s, where s is the true mean square signal level and s' the corresponding quantity derived from signals superimposed on tilting background slopes (of a rather severe 25° amplitude). From more than 1800 simulation runs, the average uncertainty and the error bar of one standard deviation are shown in Fig. 3d. Based on these results, the uncertainty of the surface curvature calculation is approximately 10% at lower wind speeds (say, $U_{10} \approx 1.3$ m s^{-1}, $s_{11} \approx 0.125$, Table 1). At higher wind velocities, the uncertainty is further reduced to be approximately 5%. For less severe background tilting, the uncertainties are proportionally reduced.

b. Ambient light

Due to the limited laser power (8 mW output, 670 nm wavelength), the signals deteriorate markedly under bright sunlight, although narrow bandpass filters are used (appendix A). A discussion of the effect of ambient light on the slope measurements is given in appendix B. It is shown that the ambient light causes an attenuation of the slope signals. The attenuation factor as a function of the ambient level normalized by the laser intensity (denoted as N/S) is shown in Fig. 4. Experiments were carried out in the laboratory to confirm the analytical calculations. The details of the experiments are also described in appendix B. The agreement between the laboratory measurements (data points shown as circles) and the analytical solution (shown as a dashed line) is excellent (Fig. 4). The attenuation effect due to ambient light in the ocean is also compared with the field data, and similar agreement with the analytical solution is found (Sletten et al. 1994). From these results, the data segments with ambient light intensity $N/S < 2$ can be compensated with reasonable confidence. The ambient intensity of the data selected for this presentation is much less, $N/S < 0.76$ (Table 1). During the data processing, the ambient light intensity is updated every 10 s.

4. Wavenumber spectra of capillary–gravity waves

The output of the scanning slope sensor allows the computation of the transect wavenumber spectra rather than the omnidirectional wavenumber spectra. With the assumption of a relatively constant directional distribution, these two sets of spectra differ by a constant proportion. Detailed discussions of the treatment for the gravity wave condition have been presented in earlier publications (e.g., Schule et al. 1971; Phillips 1977, 1985). When the spectral function is composed of segments of different slopes, such as those in the CG wave region (to be shown later), the ratio of the transect and the omnidirectional spectra can be shown to remain proportional under the assumption of a constant or slowly varying directional distribution. The magnitude of the proportionality constant is close to unity (appendix C). In the following, the wavenumber k is understood to be the component of $\boldsymbol{k}$ in the direction of laser scanning (the transect), which aligns with the primary wind direction as stated earlier.

a. Spectral features

The average curvature spectra, $\chi_{11}(k)$, of the six cases listed in Table 1 are plotted in Fig. 5a. The wave-

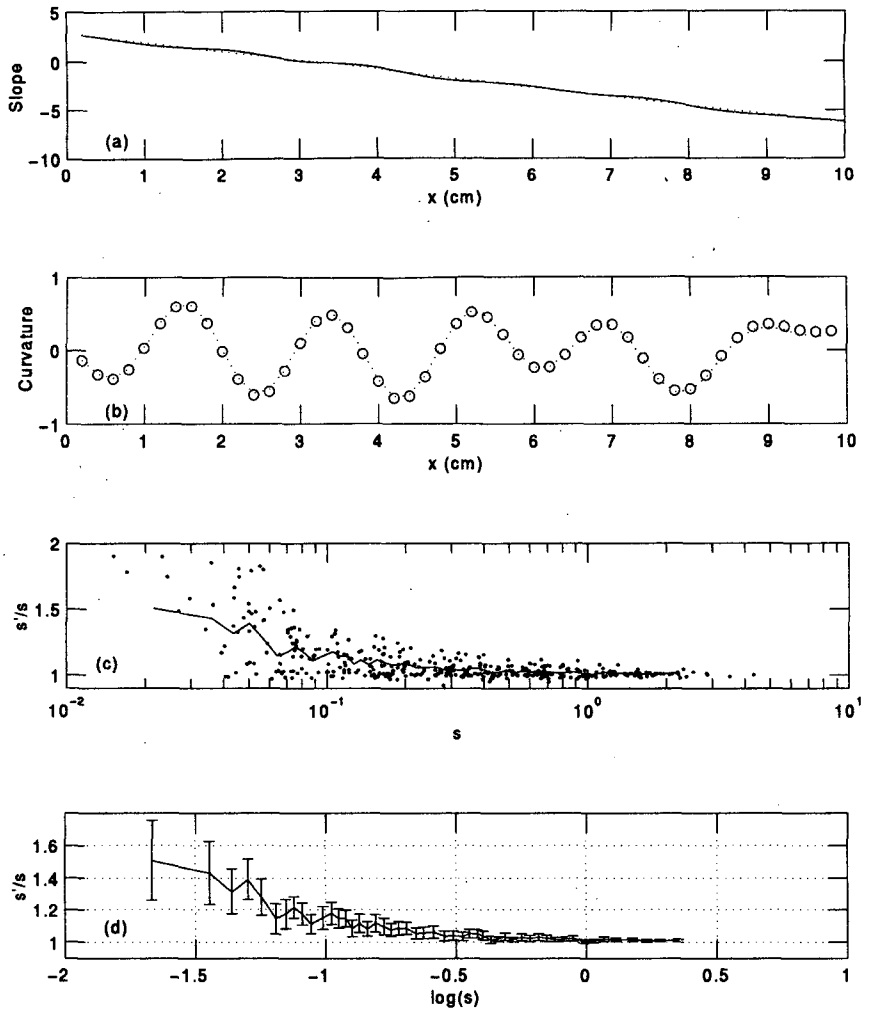

FIG. 3. Simulation examples showing the data processing procedure used to derive the surface curvature from the slope measurement on a moving frame that is subject to random tilting of ocean waves. (a) The slope signal (solid curve) composed of 40 short-wave components superimposed on a slowly varying background tilted surface. The background surface is shown as a dotted curve. (b) The derived curvature signal from finite differencing of the slope signal (○). For comparison, the true curvature of the short waves is plotted as a dotted line. (c) Examples of the expected uncertainty of the mean square curvature as a function of signal intensity. The solid curve is the average trend. (d) The average uncertainty and error bar (one standard deviation) from more than 1800 simulations.

number spectra of surface slope, $\chi_1(k)$, and of surface displacement, $\chi(k)$, can be obtained from $\chi_{11}(k)$ by multiplying with k^{-2} and k^{-4}, respectively. These spectra are shown in Figs. 5b and 5c. It is observed that when wind speeds exceed the threshold condition, the spectra of short waves show general similarities. Specifically, for the four higher wind cases ($1.3 < U_{10} < 5.7$ m s^{-1}) displayed in Figs. 5a–c, two prominent features are noticed.

1) There is a pronounced peak in the curvature spectrum. In the spectra of slope and displacement, there are corresponding "breaks" of the spectral shapes. The wavenumbers at the peaks of curvature spectra or at the break of the slope or displacement spectra are approximately constant at $k = k_p \approx 9$ rad cm^{-1}.

2) The shapes of the spectral branches on the two sides of the spectral peaks or the spectral breaks, that is, the spectral shapes in the two regions of $k \ll 9$ and $k \gg 9$ rad cm^{-1}, are reasonably smooth and can be represented by power-law functions of wavenumber k. The slopes of the two spectral branches are approximately 1 and -1 for the curvature spectra (Fig. 5a), -1 and -3 for the slope spectra (Fig. 5b), and -3 and -5 for the displacement spectra (Fig. 5c). For comparison, short line segments with slopes 1 and -1, -1

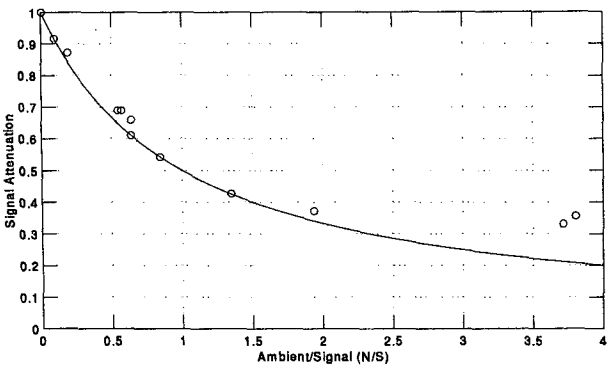

FIG. 4. Signal attenuation caused by ambient light contamination. Solid curve, analytical solution (B4); circles, laboratory measurements.

and −3, and −3 and −5 are added in Figs. 5a, 5b, and 5c, respectively.

b. Wind dependence

The wind speed dependence of the properties representative of mean-square surface roughness (curvature, slope, or displacement), averaged using the full data length listed in Table 1, is shown in Fig. 5d. The rate of increase of the CG waves with wind speed is found to be approximately linear in the range of $1.3 < U_{10} < 5.7$ m s^{-1}. For reference, a short line segment with slope 1 is also plotted in this figure.

Due to the long averaging time, this processing yielded only 4 data points representing cases when wind speeds exceed critical condition. We also processed mean-square statistics using shorter averaging time. The scatter of computed mean-square data points increases with decreasing data length, as expected from a random process. Figure 5e shows an example of the computed mean-square curvature using an averaging time of 200 s. The linear wind speed dependence is also distinctive for the data points with higher wind speeds (cases 2422, 1413, 1310, and 1223 of Table 1). Most of the data points of these four cases are confined within the factor-of-two envelopes drawn in Fig. 5e. The group of points lying about one order of magnitude below the dashed curves belong to the low wind case 1213, and case 1810 that appears to be influence by natural slicks, as discussed earlier. Further discussion of the last case is given in section 5c. It is clarified here that the mean-square roughness (curvature, slope, or displacement) presented in Figs. 5d and 5e represents the fractional contribution from the CG wave band of $1 < k < 16$ rad cm^{-1}. To obtain the total mean square of surface roughness, contributions from gravity and capillary waves outside the resolved wavenumber region will need to be accounted (Hwang 1995).

The spectral densities of individual wavenumber components for the four higher wind cases plotted in Figs. 5a–c also show a clear trend of increasing monotonically with wind speed. The trend is evident over the full range of the wavenumber resolved, $1 < k < 16$ rad cm^{-1}. Figure 5f plots the spectral density as a function of wind friction velocity. The linear wind speed dependence appears to hold for the spectral density of individual wavenumber components in most of the cases.

The result that above the threshold wind velocity the spectral densities of individual wave components increase linearly with wind speed is quite interesting. This result does not agree with measurements obtained from laboratory simulations (to be further discussed in the next section) or from microwave remote sensing. It is emphasized that almost all the available field measurements of surface slopes collected in the ocean environment show a linear wind dependence. A detailed comparison of the mean-square slopes derived from the scanning slope sensor and other datasets obtained from optical sensors and microwave radars is presented in Hwang (1995).

c. Other parameters

As mentioned earlier, scattered slick bands were noticed in the experimental regions in two cases (1810 and 2422, corresponding to the second and third lowest spectra in Fig. 5a–c). In both cases, the SSS buoy was found to cross the slick bands at least once from occasional observations when the ship was close by. Interestingly, the mean velocities of the two cases are nearly identical; the calculated U_{10} of both cases is approximately 1.3 m s^{-1}, but the two wavenumber spectra are distinctly different. We have attempted to correlated the spot observations of slick encounters with recordings from various sensors mounted on the buoy. The results are not fully satisfactory and a reliable way of identifying slick encounters from instrument recordings is not available, yet. The effect of slick damping in these two cases is therefore uncertain at this stage.

In addition to the possible slick influence, it is observed that the gustiness (as reflected in the root-mean-square wind speed fluctuation) and the stability condition (as reflected in the air–sea temperature difference) are considerably different for these two cases (Table 1). The apparent fluctuation of wind velocity and stability condition is a function of the data length used for signal processing. The determination of the *proper* averaging time is not a simple one. It is primarily determined by the relaxation characteristics of the wave components involved, as a result of short-wave modulation by surface features of various scales (e.g., Hwang and Shemdin 1990; Hwang 1992). Some of the controlling parameters determining the modulation characteristics include wind properties (speed, direction, and fluctuation), atmospheric stability conditions, surface current conditions (convection and straining), the interaction time and distance of the

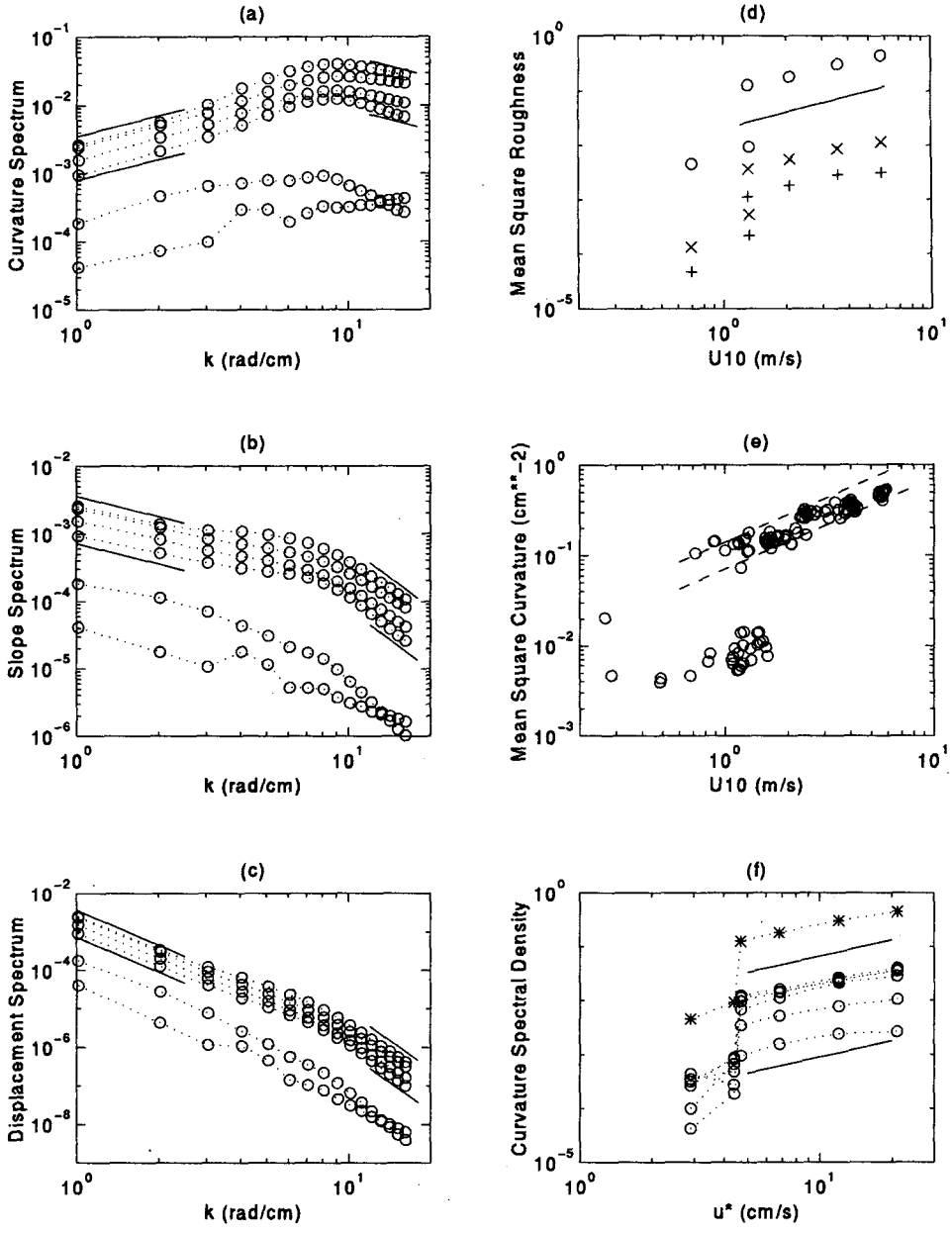

FIG. 5. The transect wavenumber spectra of short ocean waves at six wind velocities: (a) Curvature spectra. The slopes of the short line segments drawn in the regions of $k \ll 9$ and $k \gg 9$ rad cm^{-1} are 1 and -1, respectively. (b) Slope spectra. The slopes of the line segments are -1 and -3. (c) Displacement spectra. The slopes of the line segments are -3 and -5. (d) The wind speed dependence of the surface roughness statistics, represented by the mean square curvature (○), slope (×), and displacement (+). The averaging time for each case is the total data length (>1000 s), as listed in Table 1. The slope of the short line segment is 1. (e) The wind speed dependence of mean square curvature, the averaging data length is 200 s. The slope of the two line segments representing the factor-of-two envelops is 1. (f) The curvature spectral densities of individual wavenumber components plotted as a function of wind friction velocity, showing the linear relationship for cases with wind speed exceeding a threshold condition. The slope of the short line segments is 1. The spectral densities at k = 1, 3, 7, 9, 12, and 16 rad cm^{-1} are shown (○). The mean-square curvature data are also plotted in this figure (*).

wind, current and waves, and the dissipation mechanisms. The investigation of the quantitative effects on the short-wave properties due to various environmental parameters is in progress.

5. Discussion

a. The spectral function

It has been well established that the spectral coefficient for the saturation range is clearly not a universal constant, and most field observations support that the spectral density of high-frequency gravity waves increases linearly with wind speed or wind friction velocity, as mentioned earlier. This wind dependence is usually factored as (u_*/c), where u_* is the wind friction velocity and c the phase speed of the wave component. The normalization scheme is not fully supported by observations of wavenumber spectra in the gravity wave region (some of the data are cited in Phillips 1985) or by the current dataset. In this section, an attempt is made to construct an empirical spectral model using the field measurements of wavenumber spectra described in the last chapter. The dependencies of the spectral coefficient on the two velocity scales, u_* and c, are treated as uncorrelated and will be derived from the ocean data. Assuming a spectral function of the following form

$$\chi(k) \sim u_*^{\alpha} c^{\beta} k^{\gamma}, \tag{1}$$

or in dimensionless representation,

$$k^3\chi(k) = A\left(\frac{u_*}{c_m}\right)^{\alpha}\left(\frac{c}{c_m}\right)^{\beta}\left(\frac{k}{k_m}\right)^{\gamma+3}, \tag{2}$$

where c_m is the phase velocity of the wave component with wavenumber k_m and A is a dimensionless spectral coefficient. Heuristically, the formulation in (2) identifies u_* as the forcing mechanism of the wind–wave system, the properties of the generated waves are represented by the variable parameters c and k, and the fluid properties and body force of the system are characterized by the constant parameters c_m and k_m. For capillary–gravity waves, the primary environmental factors are gravity and surface tension, which are embedded in c_m and k_m.

The search for the dependence on u_* is straightforward; the linear relationship ($\alpha = 1$) is readily established from observations such as those shown in Fig. 5f. Measurements in the CG wave region offer a unique opportunity to investigate the dependence on c because the phase velocity dependence on k differs significantly in the two regions of gravity and capillary waves. Explicitly, $c^2 = gk^{-1}$ for gravity waves, and $c^2 = \tau k$ for capillary waves, where g is the gravitational acceleration, τ the ratio of surface tension T and water density ρ. The demarcation wavenumber is expected to be in the neighborhood of $k_m = g^{1/2}\tau^{-1/2}$, which is equal to 3.74 rad cm^{-1} with the substitution of $g = 981$ cm s^{-2} and $\tau = 70$ cm^3 s^{-2}. The range of wavenumbers in the present measurements, $1 < k < 16$ rad cm^{-1}, covers a reasonable span (a factor of 4) on either side of k_m. The phase speed dependence on the wavenumber introduces a change of the spectral slope in the two regions of gravity and capillary waves, so that (1) can be expressed as

$$\chi(k) = \begin{cases} A_1 u_* g^{\beta/2} k^{\gamma-\beta/2}, & k \ll k_m \\ A_2 u_* \tau^{\beta/2} k^{\gamma+\beta/2}, & k \gg k_m \end{cases} \tag{3}$$

or

$$\chi_{11}(k) = \begin{cases} A_1 u_* g^{\beta/2} k^{4+\gamma-\beta/2}, & k \ll k_m \\ A_2 u_* \tau^{\beta/2} k^{4+\gamma+\beta/2}, & k \gg k_m, \end{cases} \tag{4}$$

where A_1 and A_2 are dimensional, absorbing the constant parameters k_m and c_m. From the wavenumber spectra of CG waves, the exponent β can be derived from the slope change in the two spectral branches on the two sides of the peak wavenumber, that is,

$$\beta = s_c - s_g, \tag{5}$$

where s_c and s_g are respectively the spectral slopes in the capillary and gravity regions. This relationship holds whether one uses the spectra of displacement, slope, or curvature to derive the spectral slopes as long as the wavenumber range covers both capillary and gravity regions. As discussed earlier, from the results of the curvature spectra shown in Fig. 5a, $s_g = 1$, $s_c = -1$, and $\beta = -2$. This result coupled with the observation of apparent spectral slope determines the exponent γ to be -4. Substituting these exponents into (2), the wavenumber spectrum can be written as

$$\chi(k) = A\left(\frac{u_*}{c}\right)\left(\frac{c_m}{c}\right)k_m k^{-4}. \tag{6}$$

The dimensionless spectral coefficient A may have different numerical values in the gravity and capillary regions. This can be seen from rewriting (6) as

$$\chi(k) = \begin{cases} A_g g^{-1} u_* c_m k_m k^{-3}, & \text{gravity waves} \\ A_c \tau^{-1} u_* c_m k_m k^{-5}, & \text{capillary waves.} \end{cases} \tag{7}$$

At the *matching* wavenumber, presumably k_p, the two expressions on the right-hand side of (7) must be equal. Therefore, $A_c/A_g = k_p^2\tau/g$. The ratio would be unity if the wavenumber where the two spectral segments match is k_m. However, the observed spectral peak in the curvature spectra is much higher (Fig. 5a) at $k_p = 9$ rad cm^{-1} and is found to be relatively independent of wind speed. It is not immediately clear why the spectral peak does not vary with wind (although the reported wind speed is on the low side, the covered range from 1.3 to 5.7 m s^{-1} represents a factor of more than 4) and what the significance is of such a peak wavenumber corresponding to a wavelength of 0.7 cm.

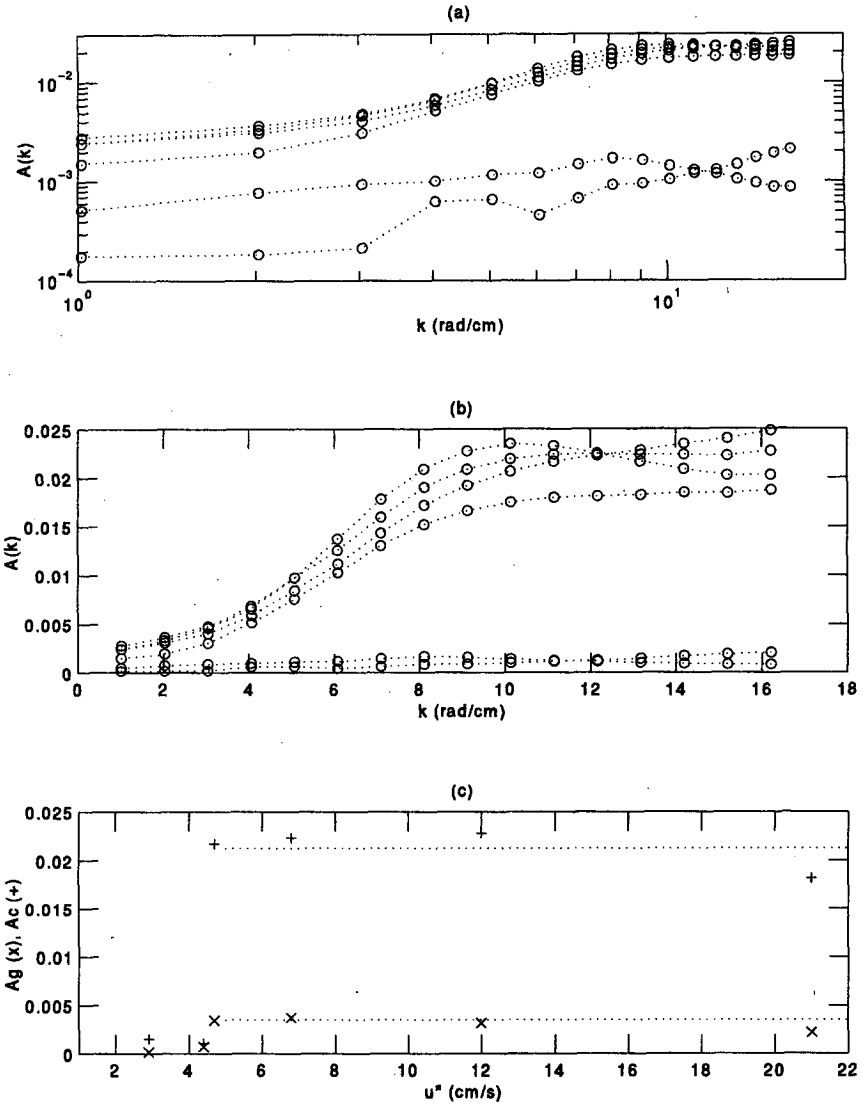

FIG. 6. (a) The dimensionless spectral coefficient calculated from the measured curvature wavenumber spectra showing the asymptotic trend in the gravity and capillary wave regions. (b) Same as (a) but plotted in linear scale. (c) The mean values of the dimensionless spectral coefficient: ×, gravity wave region; +, capillary wave region.

Some possible implications on wave generation mechanisms based on these observations are discussed in the next section. In any case, based on the observed spectral peak location, the ratio A_c/A_g is expected to be approximately 5.8.

Empirically, the dimensionless spectral constant A can be calculated from the measured spectra according to (6). The results are shown in Figs. 6a and 6b. The magnitude of A (for wind speeds exceed threshold condition) approaches a constant value in either end of the CG wave spectrum, as suggested by (7). The capillary asymptote, A_c, can be evaluated from the average over the high wavenumber end of the spectra. Figure 6c shows the results calculated from the average of the last seven wavenumber components ($k \geq 10$ rad cm^{-1}). The variation of A_c with the wind friction velocity is found to be small for cases with $U_{10} > 1.3$ m s^{-1} ($u_* > 4.7$ cm s^{-1}). The mean value of A_c with one standard deviation is $2.1(\pm 0.11) \times 10^{-2}$.

In the gravity wave region, the calculated $A(k)$ (Figs. 6a,b) appear to be just approaching the gravity asymptote, A_g. The spectral coefficients corresponding to the first wavenumber component ($k = 1$ rad cm^{-1}) are considered representative of A_g and also plotted in Fig. 6c. Again, the variation with wind condition of these empirically derived asymptotic spectral coeffi-

cients is small. The mean value with one standard deviation is $2.3(\pm 0.55) \times 10^{-3}$.

The ratio of the observed ratio of A_c/A_g is 9.2 ($\pm 30\%$), as compared to the value 5.8 calculated in the last paragraph. For engineering applications, the spectral coefficient can be approximated using the following three-branch empirical equation:

$$A = \begin{cases} 2.3 \times 10^{-3} = A_g, & k \leq 1 \text{ rad cm}^{-1} \\ 8.6 \times 10^{-3} k_m^{-1}, & 1 < k \leq 9 \text{ rad cm}^{-1} \\ 2.1 \times 10^{-2} = A_c, & k > 9 \text{ rad cm}^{-1}. \end{cases} \quad (8)$$

Table 2 lists the numerical values of $B_g = A_g g^{-1} u_* c_m k_m$ and $B_c = A_c \tau^{-1} u_* c_m k_m$ for a range of wind friction velocities. At $u_* = 30$ cm s^{-1}, the gravity wave spectrum is $6 \times 10^3 k^{-3}$. It is noted that the wind speed conditions in the present dataset cover only $u_* < 21$ cm s^{-1}; more field measurements are needed to confirm the extension of these results to higher wind speeds.

b. *Mechanisms of capillary wave generation on the ocean surface*

The peculiarities in the wave spectra described in the last section may be related to the generation mechanisms of capillary–gravity waves. Three major sources are generally considered important for the generation of short waves on the water surface: wind, steep gravity waves, and breaking waves. At the low wind speed conditions encountered in the present experiment, the mechanism of wave breaking is not expected to be dominant. The wind generation appears to be a primary contributor as demonstrated in Fig. 5, which shows that both the mean-square statistics and the spectral densities of individual components (in the range of resolved wavelengths) increase linearly with wind speed. The observations that the peaks of the curvature spectra occur at a wavenumber considerably higher than that corresponding to the slowest moving wave component ($k_p = 9$ rad cm^{-1} vs $k_m = 3.74$ rad cm^{-1}) and that k_p is independent of wind speed (at least within the present experimental range U_{10} from 1.3 to 5.7 m s^{-1}) are somewhat puzzling and may suggest that other nontrivial generation mechanisms of short capillary waves exist in addition to direct wind forcing. Two of these mechanisms may be the generation of capillary waves by high curvature and vortices near the crests of underlying gravity waves, as analyzed by Longuet-Higgins (1963, 1992). Capillary wave generation at the steep wave crest without blowing wind has been demonstrated in the experiments of Cox (1958). More recent high-speed imaging of capillary waves generated by steep gravity waves (Perlin et al. 1993) also demonstrates the prevalence of capillary waves in the company of short gravity waves and with the absence of wind. Because steep gravity waves maintain a geometric similarity at the crest, namely, the Stokes 120° inclusion angle, the generated capillary waves also display geometric similarity.

If the capillary wave generation by crests of short gravity waves is an important process in addition to direct wind forcing, the CG waves on the ocean surface represent an image of the underlying short gravity waves, mainly of those crests with high curvature. The spectral intensity and modulation characteristics of the CG waves then reflect the same properties of the short gravity waves. Interestingly, similar observations have been reported in the microwave remote sensing of the ocean surface, where the images from *X*-band and *K*-band radars with Bragg wavelengths in the CG wave region are found to be very similar to the images from *L*-band radars with Bragg wavelengths on the order of 25 cm (e.g., Hughes and Gower 1983; Thompson and Gasparovic 1986). Indeed, one of the most successful models of microwave modulation in the *X*-band needs to take into account the broadening of the Bragg wavenumber from tilt modulation due to gravity waves of intermediate wavelengths, of order 1 m (Thompson 1988). Of course, the radar backscatter modulation involves more than hydrodynamic modulation and depends on many other parameters including incident angle, azimuthal angle, surface tilting effect, and non-Bragg-scattering mechanisms attributed to wave breaking and ill-defined geometric conditions such as wedges and discontinuities at the water surface. The subject is beyond the scope of this article.

Close inspection of wind wave generation in a water body such as a lake or a harbor shows that the short wind waves are rarely two-dimensional. When disturbed by wind, the surface oscillates with waves of different length scales. Frequently, numerous wave crests (with a feature length scale on the order of 20 cm) surge up, pushing in front of them a group of capillary waves with subcentimeter wavelengths. This process is obviously different from the high curvature generation (Longuet-Higgins 1963) discussed earlier because the surface of these surging crests remain

TABLE 2. Calculated magnitude of spectral coefficients as a function of wind friction velocity.

	Magnitude									
u_* (cm s^{-1})	5	10	15	20	25	30	35	40	45	50
B_G ($\times 10^{-3}$)	1	2	3	4	5	6	7	8	9	10
B_C	0.13	0.26	0.39	0.51	0.64	0.77	0.90	1.03	1.16	1.29

rounded and smooth beneath the capillaries. The mechanism is probably more akin to the generation process of capillary waves by obstacles in a running stream or by an object moving in stationary water (Lighthill 1979). In other words, because the high speed of the surging motion, the surging crests behave temporarily like solid objects moving against the surrounding water. This surging motion obviously contributes to the development of the three-dimensional structure on the water surface. At lower wind speeds near the threshold condition, the surging crests with attached capillaries appear in discrete and isolated locations. As the wind speed increases further, the crests cross each other, forming a diamond pattern. At some particular wind speed, the water surface appears to be covered densely with little dimples, sometimes referred to as cat's paws (Kinsman 1965). As wind slackens, the short capillary waves die down almost instantaneously, but the decimeter waves remain. This is due to the great difference of the modulus of decay of water waves as a function of wavelength, $(2\nu k^2)^{-1}$, where ν is the kinematic viscosity of water (Lamb 1945). The decay timescale is calculated to be more than 20 min for waves with a 30-cm wavelength, and 0.5 s for a 0.63-cm wavelength. As mentioned earlier, the spectra measured in the ocean display a peak wavenumber near $k = 9$ rad cm^{-1}. The wavelengths of the capillary waves generated by the surging crests appear to be rather constant, estimated to be between 0.5 and 0.8 cm ($k = 12.5$ to 7.9 rad cm^{-1}) and much shorter than the wavelength ($\sim$1.7 cm) corresponding to the surface wave component with minimum phase velocity. It is possible that the generation of capillary waves by surging crests as described above is also an important dynamic process at the air–water interface.

c. *Comparison of field data and laboratory measurements*

In this section we compare the field data with laboratory measurements, which usually extend to much higher wind conditions. Of particular interest to this study are the spatial measurements of Jahne and Riemer (1990), obtained in a large tank at a 90-m fetch by imaging a two-dimensional underwater light source with a "coded" intensity pattern, and of Hwang et al. (1993), obtained at 16-m fetch by a linear scanning slope sensor operating on the same optical refraction principle as that used in the system discussed in this article. A summary of the wind conditions and short-wave properties is given in Table 3.

It is found that the characteristics of the spectra collected from the ocean are very different from those obtained in the laboratory. The differences include nearly all the major features of wave spectra, notably, the spectral density level, the threshold wind condition, the wind dependence of individual spectral components, the apparent spectral slope, and the variation of spectral slopes in the gravity and capillary regions. These observations are summarized in Fig. 7, in which the short-wave properties in the wavenumber range between 1 and 16 rad cm^{-1} are compared. In the first three panels (Figs. 7a–c), the statistics of mean-square (MS) curvature, slope, and displacement, integrated from the spectra reported in the cited papers, are graphed with respect to the wind friction velocity. The field data consistently show that the wind dependence of the mean square properties of short waves is close to linear, while the wind dependence of the laboratory data is somewhat steeper than square in the MS curvature measurements and somewhat less than square in the MS displacement results. For convenience of comparison, line segment with slope 1 (solid) and 2 (dashed) are added in Figs. 7a–c. It is emphasized that over the past 40 years almost all the field data on the mean-square slope collected in the ocean since Cox and Munk (1954) have shown a linear wind dependence (Hwang 1996).

As discussed earlier, for the field data, the wind dependence of individual spectral components is also linear. Such a simple relationship was not found in the laboratory data. The details are presented in the original papers (Jahne and Riemer 1990; Hwang et al. 1993).

TABLE 3. Summary of the wind conditions and short-wave properties of the comparison datasets.

(a) Field data (High Resolution ARI Experiment)						
U_{10} (m s^{-1})	0.84	1.33	1.31	2.08	3.54	5.72
u_* (cm s^{-1})	2.9	4.4	4.7	6.8	11.9	20.5
s_{11} (cm^{-2})	0.005	0.008	0.125	0.184	0.308	0.467
s_1 ($\times 10^{-3}$)	0.13	0.52	3.63	5.45	8.50	11.26
s (cm^2, $\times 10^{-3}$)	0.048	0.22	1.11	1.82	2.79	3.10
(b) Laboratory (Jahne and Riemer 1990)						
U_{10} (m s^{-1})	2.7	3.9	5.4	7.3	8.9	12.2	17.2
u_* (cm s^{-1})	7.3	10.0	14.0	20.5	26.9	42.4	72.2
s_{11} (cm^{-2})	0.057	0.044	0.079	0.301	0.547	1.301	1.477
(+)	0.051	0.040	0.076	0.298	0.544	1.292	1.466
s_1 ($\times 10^{-3}$)	33.4	21.2	18.5	21.9	29.5	72.9	96.8
(+)	2.3	2.1	3.5	11.6	19.3	48.9	66.2
s (cm^2, $\times 10^{-3}$)	278.1	162.1	126.2	75.2	75.7	154.9	198.1
(+)	0.8	0.7	1.0	2.5	3.5	9.6	14.0
(c) Laboratory (Hwang et al. 1993)						
U_{10} (m s^{-1})	3.19	5.50	8.05	9.95	12.34	14.80
u_* (cm s^{-1})	11	17	26	33	43	54
s_{11} (cm^{-2})	0.017	0.073	0.184	0.360	0.531	0.555
s_1 ($\times 10^{-3}$)	1.7	4.7	8.8	17.0	28.6	32.4
s (cm^2, $\times 10^{-3}$)	1.1	2.2	2.9	4.9	9.3	12.0

(+) In (b) the top row is the sum of spectral density over the wavenumber range $0.3 < k < 16$ rad cm^{-1}; the bottom row is the sum of spectral density over the truncated wavenumber range $1.2 < k < 16$ rad cm^{-1}. As discussed in Jahne and Riemer (1990), the measurements in the lowest wavenumber components, say $k < 1$ rad cm^{-1}, may be contaminated by the gravity waves near the peak of the displacement spectrum.

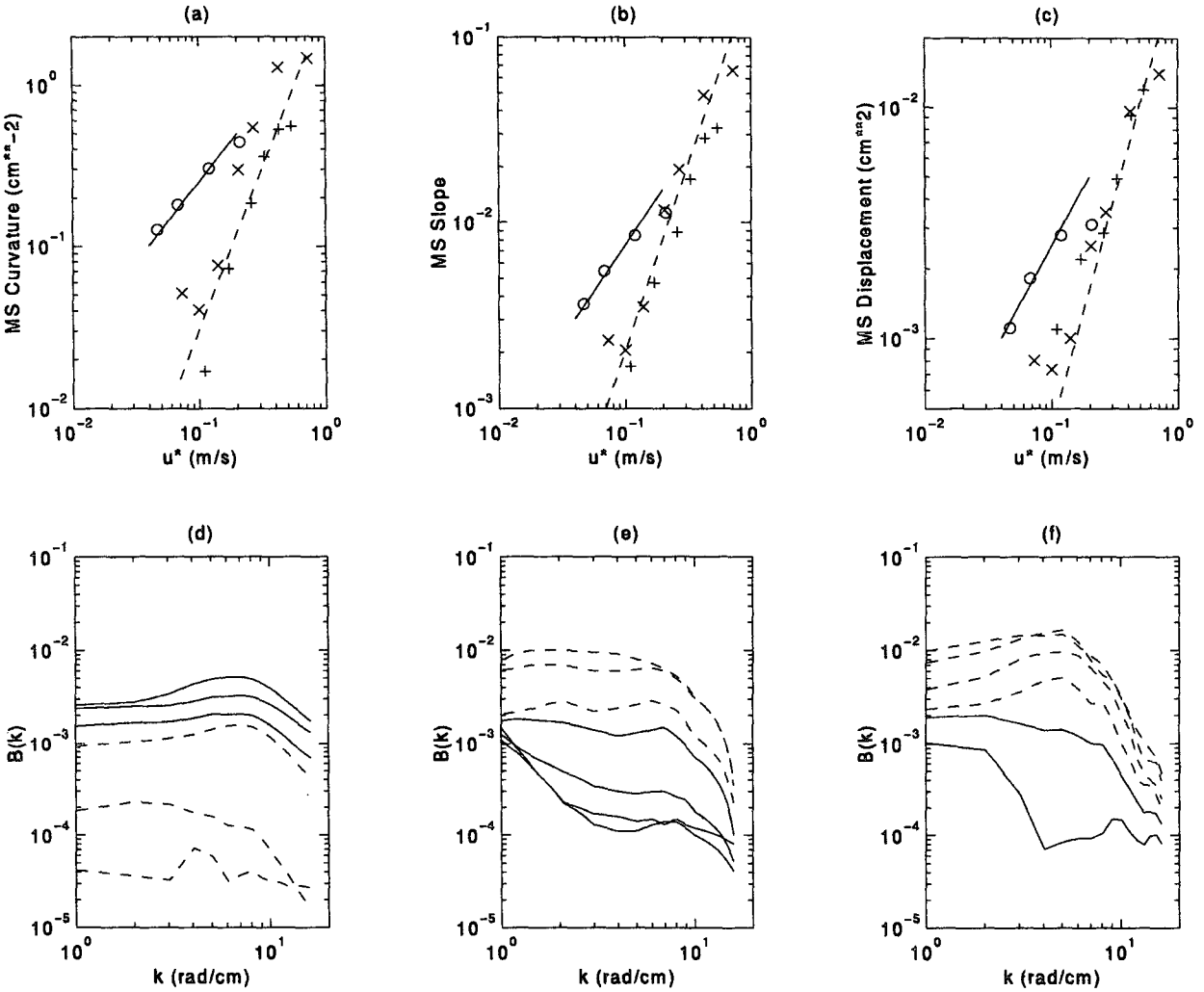

FIG. 7. Comparison of field data and laboratory measurements. Average properties for the wavenumber range $1 < k < 16$ rad cm^{-1}: (a) Mean-square curvature; (b) Mean-square slope; (c) Mean-square displacement. Symbols are ○: field data from the High Resolution Experiment, ×: laboratory (Jahne and Riemer 1990), +: laboratory (Hwang et al. 1993). The slope of the solid curve is 1, the slope of the dashed curve is 2. Spectral distribution in terms of $B(k)$: (d) Field data; (e) Laboratory (Jahne and Riemer 1990); (f) Laboratory (Hwang et al. 1993). Solid curves represent cases with overlapping wind friction velocities among the three datasets (the wind conditions are listed in Table 3).

Other characteristics of the short-wave spectra in the two environments are also significantly different, as illustrated in Figs. 7d–f [shown in terms of the degree of saturation, $B(k) = k^{-1}\chi_{11}(k)$]. In these figures, the spectra with overlapping wind friction velocities (Table 3) are plotted with solid curves. The most striking feature of the laboratory spectra is the presence of a spectral gap in the vicinity of the wavenumber corresponding to the minimum phase velocity of surface waves ($k_m = 3.74$ rad cm^{-1}), most pronounced at lower wind conditions. There have been suggestions that this spectral gap is the result of wave damping due to the presence of residual slicks on the water surface. While residual slicks may be one of the factors contributing to the differences of the properties of short waves from the two environments, there are at least three reasons to believe that other processes are responsible for the observed feature of a spectral gap near k_m: 1) In both laboratory experiments cited here, the measurement stations were more than 10 m from the downwind end of the respective facilities. The measurements were performed after a sufficient time lag (on the order of 20 min) from the start of wind to allow waves to build up to equilibrium. During this period, the surface slicks were most likely swept to the downwind end of the tanks. Furthermore, that the spectral gap exists in wind conditions up to 7 m s^{-1}, as shown in the results of Jahne and Riemer, suggests that residual slick damping is not a likely explanation of the observed feature. 2) While the exact mechanisms of wave damping by sur-

factants are still under intensive investigation, theoretical calculations show that the damping effect by slicks is most pronounced for short gravity waves in the decimeter wavelength region rather than short capillary or capillary–gravity waves. The damping effect of the surfactant depends strongly on the dynamic surface dilational viscosity, which is expected to be wind dependent (e.g., see Huhnerfuss 1986; Huhnerfuss et al. 1994). The spectral gaps in the laboratory spectra, however, exist only at the close neighborhood of k_m and with the peak effect apparently occurring at k_m (Figs. 7e, f). 3) The water quality in the field is certainly dirtier than that in the laboratory, but the distinct feature of spectral gaps shown in the laboratory spectra is not found in the ocean data (Fig. 7d).

In fact, the possibility of a spectral gap in the wavenumber spectrum had been predicted by Phillips more than a decade ago (Phillips 1985, p. 523). The physical explanation was identified to be the suppression (blockage) of short waves by surface current (Banner and Phillips 1974; Phillips and Banner 1974). Based on this mechanism, the wave component with the slowest phase speed will be affected the most, in agreement with the laboratory observations. The spectral gap was not found in the field data and at higher wind velocities in the laboratory cases. It is possible that, in order to set up the condition for *persistent* suppression of short waves in a given band, a relatively steady condition (both in speed and in direction) needs to be maintained. The wind field in the ocean, even in a very calm situation, was not steady enough (Table 1) for the persistent suppression of a fixed band of wave components; therefore, a spectral gap is not found in the average spectra. Undoubtedly, blockage still occurs in the field; due to the variation of the surface drift current as a result of wind fluctuation, a broad band of wave components is affected. This situation will not produce a distinct gap in the wavenumber spectrum. Similarly, at higher wind velocities in the laboratory the unsteadiness of wind destroys the condition for persistent suppression of a fixed band of short waves, and the spectral gap again disappears. It is postulated that a realistic fluctuation of the wind conditions is critical for the successful simulation of short-wave properties in the laboratory. Ironically, designers of most wind–wave facilities strive to produce steady wind conditions in the laboratory; this may be why the generated fine structure bears little resemblance to the counterpart from the ocean. Although it is probably not practical to try to introduce wind direction fluctuation in a wind–wave tank due to the possibility of introducing objectionable sidewall effects, the simulation of wind speed fluctuation is feasible. The resulting CG wave structure is expected to be considerably different from those reported in Jahne and Riemer (1990) and Hwang et al. (1993) and likely to be more representative of the fine structure on the ocean surface. It is also worthwhile to point out that, for short-wave measurements in the laboratory, a longer fetch, beyond say 15 m, is probably not critical. As illustrated in Fig. 7, the spatial measurements of short waves at 16 and 90 m are very similar in most features of significance.

6. Summary

Spatial measurements of capillary–gravity waves in the ocean were obtained by an optical scanning slope sensor mounted on a free-drifting buoy. The free-drifting operation minimizes flow disturbance to the sampling area and provides wind velocity measurements relative to the moving surface, which is dynamically more relevant to the short-wave generation than the wind velocity measured relative to a fixed coordinate system. The difference may be very important in the present dataset collected under relatively low wind conditions, with the range of U_{10} between 0.8 and 5.7 m s^{-1}.

The wavenumber spectra of surface curvature in the transect of wind direction were calculated from the spatial measurements of surface slopes of ocean waves. The range of wavenumbers resolved is between 1 and 16 rad cm^{-1}. The distinctive features of these spectra include the following:

1) A pronounced spectral peak exists near $k \approx 9$ rad cm^{-1}; and the peak wavenumber is found to be independent of wind speed.
2) On either side of the spectral peak, the slope of the curvature spectra is approximately constant and is observed to be 1 in the gravity region and -1 in the capillary region.
3) The spectral density increases linearly with wind speed or wind friction velocity.

These observations suggest that the spectral function is of the form $\chi(k) = A(u_*/c)(c_m/c)k_m k^{-4}$. An empirical spectral function (6) based on the ocean data is presented. The dimensionless spectral coefficient A assumes two different asymptotic values toward the gravity (0.0023) and capillary (0.021) domains. An empirical equation for the spectral coefficient for the intermediate range is given in (7).

The observations of certain unexpected features of the wavenumber spectra (the peak wavenumber of the curvature spectra, k_p, occurs at a rather high value of 9 rad cm^{-1} and appears to be independent of wind velocity) suggest that, in addition to wind forcing, other generation mechanisms may be important. Three of the mechanisms include the generation of capillaries by high curvature and vortices near the crests of underlying steep gravity waves (Longuet-Higgins 1963, 1992) and a transient process tentatively called "surging motion." The latter refers to the phenomenon of some surface features (surging crests) that lunge forward at a relatively high speed, creating a group of capillaries on the forward face of these distorted forms. This process is similar to the generation of waves by an ob-

stacle in moving water. The range of wavenumbers of the generated capillaries appears to be very narrow and is estimated to be in the vicinity of 7 to 13 rad cm^{-1}.

A comparison of the field data with laboratory measurements is presented. Significant differences in many important features of short-wave properties exist between the datasets from the two environments. The hypothesis is put forth that the fluctuation of the wind field is an important feature in the open ocean and ultimately controls the spectral characteristics of the fine structure on the ocean surface. Laboratory facilities that emphasize the suppression of wind fluctuation eliminate an important parameter of the natural conditions and produce short waves with very different signatures from those in the open ocean.

Acknowledgments. Funding for the development and fabrication of the SSS buoy was provided by the Naval Research Laboratory under Contracts N00173-91-M-7062, N00173-91-M-E801, and N00173-92-M-2889 and by a QUEST IR&D fund. The High Resolution ARI study was sponsored by the Office of Naval Research under Contract N00014-93-C-0083. Design and construction of the SSS buoy were assisted by engineers and technicians at QUEST Integrated, Inc., and the Naval Research Laboratory. Help from the officials and crew of R/V *Columbus Iselin* and from fellow investigators during the field experiment is gratefully acknowledged. The humidity data used for the computation of the wind friction velocity is provided by Jim Edson of Woods Hole Oceanographic Institute. The authors would like to thank Professor O. M. Phillips for the constructive discussions and suggestions on the data analysis of wind–wave generation mechanisms. The completion of this manuscript is partially supported by a QUEST IR&D fund.

APPENDIX A

Supplemental Information on the Sensors and Platform

a. Wind sensor

The wind sensor is a Model 5106 marine model wind monitor manufactured by R. M. Young Company. The sensor has a four-blade propeller to measure wind speed and a wind vane to measure wind direction. The propeller diameter is 18 cm, the total length of the sensor is 55 cm, and the turning radius of the balanced vane is 38 cm. The technical specifications from the manufacturer indicate that the threshold sensitivity is 1 m s^{-1} at 10° displacement and 1.5 m s^{-1} at 5° displacement. The damped natural wavelength is 7.4 m and the undamped wavelength is 7.2 m. The propeller rotation produces an AC sine wave signal with a frequency proportional to the wind speed, and three complete sine wave cycles are produced for each propeller revolution. The output frequency is 0.098 m s^{-1} per Hz or 0.00490 m s^{-1} per rpm. An interface circuit (Model 5603) converts the rpm to voltage, such that the output analog signal is linearly proportional to the wind speed (0 to 5 volts corresponds to 0 to 50 m s^{-1}). The propeller is accurate to within 2% according to the instrument manual. The vane direction is transmitted by a 10 k ohm precision conductive plastic potentiometer. The output signal is an analog voltage proportional to the azimuthal angle (0 to 5 volts corresponds to 0° to 360°).

b. Pressure sensor

The pressure sensor is a model ST2015G2 sensor with a built-in amplifier, manufactured by SenSym. The operation range is from 0 to 15 psig. An interface circuit was built in-house to adjust the offset of the voltage output. The conversion factors based on static calibrations are 1 volt equals 3.35-m water elevation for one sensor and 2.5 m for a second unit. The resolution of these two units is somewhat coarse and introduces an uncertainty of approximately 10% on the conversion of the surface slope. The formulas for the slope conversion based on Snell's law are discussed in detail in Hwang et al. (1993). In a subsequent revision, an amplifier circuit was built to increase the sensitivity by a factor of 8 in one unit and a factor of 32 for the other unit. The improved system was deployed in a second trip during September–October 1994.

c. Accelerometer

The accelerometer is a model 348A09 Isolator Accelerometer with an extended low-frequency response, manufactured by PCB Piezotronics, Inc. The operation range is ±50 g with a sensitivity of 0.1 volt g^{-1}. After the High Resolution ARI experiment, one of the two accelerometers was replaced by a more sensitive model with 10 volts g^{-1} sensitivity (Model 393B12 Seismic Accelerometer).

d. Thermometer

The water temperature is measured by an Endeco Type 1189 Water Temperature Probe, and the air temperature is measured by an Endeco Type 1165 Air Temperature Probe with a self-aspirating solar radiation shield. The range of output is 0 to 5 volts corresponding to −5° to 45°C. The error in the measurements is less than ±0.05°C in the range of 10° to 35°C based on the calibration sheets supplied by the manufacturer.

e. Compass

The orientation of the buoy frame is monitored by an electronic compass, Model C100, manufactured by KVH Industries, Inc. The analog port provides a 0.1–1.9 volt linear output corresponding to 0 to 360 de-

grees. The resolution of the voltage output is 4 mV. The compass reading is used to derive the wind direction. The response of the buoy (with a wind vane installed) to a turning wind can be obtained from the direction output of the Young wind sensor. Ideally, if the buoy follows the wind as fast as the wind sensor does, the direction output from the wind sensor will be a constant. Examination of the data from ocean deployments indicates that, under normal conditions, the standard deviation of the output wind direction (averaged over 10 s) from the wind sensor is typically a few degrees, indicating that the buoy platform is responding to wind direction closely.

f. Components of slope sensor

The position sensor used to measure the instantaneous position of the refracted laser beam is a lateral-effect diode (Model PIN-SD/50) manufactured by United Detector Technology (UDT). The frequency response of the sensor is 70 kHz, based on the manufacturer's specifications. Designed for a dynamic range of $\pm 34°$ surface slope, a frosted glass with a diameter of 25 cm is used as the scattering surface for imaging. A 50 mm, f1.4 camera lens is used to focus the optical image into the two-dimensional position sensor, which has a sensing surface 4.45 cm (1.75 inches) in diameter. A bandpass optical filter, composed of a pair of high-pass and low-pass interference edge filters (Corion LL-650 and LS-700), is placed in front of the camera lens to filter out unwanted ambient light. The bandwidth of the filter is 50 μm centered at 675 μm; the wavelength of the diode laser used as the optical source is 670 μm. The signals from the position sensor are processed through two UDT 301DIV-30 kHz amplifiers to produce the (x, y) position output. The frequency response of the system is limited by the A/D hardware (20 kHz) available for the AMPRO computer at the time of system fabrication (1991). Using two A/D interface cards, this A/D speed is sufficient for the original design of one-dimensional scanning with a 5 ms line-repetition period (the actual period is 4.3 ms in the final setting, of which the optical scanning period is 2.5 ms with 50 positions sampled along each scan line, and the remaining time is used for collecting measurements from other sensors at a lower speed).

g. Instrument platform

To achieve a light weight and low disturbance, a triangular scaffold is used to serve as the skeleton of the scanning slope sensor buoy, which serves also as the instrument platform for all the sensors. Thin steel cables are stretched across the vertical members to increase the stiffness of the overall structure. Horizontal flotation bars are distributed along the three sides of the triangular structure and placed at 30 cm beneath the mean water level to prevent disturbing the water surface. The only members that pierce through the water surface are three aluminum tubes, 3.81 cm (1.5 inches) in diameter. The diameter of the tubes is increased to 10 cm at the water line with the addition of flotation placed near the water surface to provide restoration in response to heaving and pitching. Each side of the triangle is 1 m wide, and the minimum distance of any vertical member to the edge of the optical sensing region is 54 cm, which is more than five diameters away from the disturbance source; we expect the flow disturbance from the framework to be reasonably small. The disturbance is further reduced by a wind vane to steer the instrument platform so that one of the open faces of the triangular structure points in the upwind direction, opening up the distance between wakes from the vertical members to the optical sensing area. Finally, the flow disturbance can be reduced to a minimum when the relative velocity between the structure and the surface water is minimized, which can be achieved with a free-drifting operation.

APPENDIX B

Compensation of Ambient Light Contamination

The position sensor used in the scanning slope sensor is a lateral-effect diode (appendix A), which obtains the position of the refracted laser beam from the induced currents on a pair of terminals located on the two opposite ends of the sensing element. For a two-dimensional position sensor, two pairs of terminals are used. The position x in one axis can be derived from

$$x = \frac{I_2 - I_1}{I_2 + I_1}, \tag{B1}$$

where I is the induced current, and the subscripts 1 and 2 represent quantities measured at the two terminals. With ambient noise, the measured position becomes

$$\hat{x} = \frac{(I_2 + n_2) - (I_1 + n_1)}{(I_2 + n_2) + (I_1 + n_1)}, \tag{B2}$$

where n is the noise induced by ambient light. If the ambient noise is uniformly diffused, a reasonable assumption for a downward-looking receiving unit with a frosted glass as the image plane (appendix A), the induced noise can be considered as isotropic, $n_1 = n_2 = N/2$. Substituting into (B2), one obtains

$$\hat{x} = \frac{I_2 - I_1}{I_2 + I_1 + N}. \tag{B3}$$

Normalized by (B1), it is shown that the ambient light introduces an attenuation to the signal

$$\frac{\hat{x}}{x} = \frac{I_2 + I_1}{I_2 + I_1 + N} = \frac{S}{S + N} = \frac{R}{R + 1}, \tag{B4}$$

where $S = I_2 + I_1$ is the signal intensity and $R = S/N$ is the signal to noise ratio. The function is plotted in Fig. 4.

To confirm this result, laboratory measurements were conducted in which the variable ambient light intensity was provided by a few lightbulbs projected onto a diffusing surface. The response of the position sensor was determined by the output of the laser beam scanning a span of 6 cm as a function of the variable ambient light intensity. It can be shown that the attenuation effect on the output of a given position span as empirically measured also follows (B4). The experimental results are also plotted in Fig. 4. The agreement between the analytical solution and the experimental data is excellent.

APPENDIX C

Transect Wavenumber Spectra in the Capillary–Gravity Wave Region

The wavenumber spectrum $\chi(k_1)$ derived from a linear-scanning laser slope sensor differs slightly from the omnidirectional spectrum $\chi(k)$ derived from the two-dimensional spectrum $\Psi(\boldsymbol{k})$. In this appendix, $\boldsymbol{k}$ is the wavenumber vector with magnitude k, and k_1 is the component in the transect (scanning) direction (the variables used in this appendix are defined differently from those used in the main text of this article). The two spectra can be written as

$$\chi(k_1) = \int_{-\infty}^{\infty} \Psi(\boldsymbol{k}) dk_2 \tag{C1}$$

and

$$\chi(k) = \int_{-\pi}^{\pi} \Psi(\boldsymbol{k}) k d\theta, \tag{C2}$$

where k_2 is the wavenumber component orthogonal to k_1 and θ is the wave direction. The present discussion follows the treatment of Phillips (1985, p. 519) but also considers the case of multiple spectral slopes:

$$\Psi(k) = \begin{cases} A_1 k^{-a_1} \cos^{p_1}\theta, & k < k_p \\ A_2 k^{-a_2} \cos^{p_2}\theta, & k > k_p. \end{cases} \tag{C3}$$

Since $k_2 = k_1 \tan\theta$, (C1) can be written as

$$\chi(k_1) = k_1 \int_{-\pi/2}^{\pi/2} \Psi(\boldsymbol{k}) \cos^{-2}\theta d\theta. \tag{C4}$$

The integration of (C4) in the region with uniform spectral slope, that is, $k_1 > k_p$ is straightforward. With the substitution of the second part of (C3), the following equation is obtained:

$$\chi(k_1) = A_2 k_1^{1-a_2} I(a_2 + p_2 - 2), \quad k_1 > k_p, \tag{C5}$$

where

$$I(x) = \int_{-\pi/2}^{\pi/2} \cos^x\theta d\theta. \tag{C6}$$

For $k_1 < k_p$, the integration in (C4) becomes

$$\chi(k_1) = 2k_1 \left\{ A_1 \int_0^{\theta_p} \cos^{p_1}\theta \cos^{-2}\theta (k_1^2 + k_2^2)^{-a_1/2} d\theta + A_2 \int_0^{\theta_p} \cos^{p_2}\theta \cos^{-2}\theta (k_1^2 + k_2^2)^{-a_2/2} d\theta \right\}. \tag{C7}$$

With some algebraic manipulations and the assumption that $p_1 = p_2 = p$, the following is obtained:

$$\chi(k_1) = A_1 k_1^{1-a_1} I_p(a_1 + p - 2) + A_1 k_p^{a_2-a_1} k_1^{1-a_2} I_{p*}(a_2 + p - 2), \quad k_1 < k_p, \tag{C8}$$

where

$$I_p(x) = 2 \int_0^{\theta_p} \cos^x\theta d\theta \tag{C9}$$

$$I_{p*}(x) = 2 \int_{\theta_p}^{\pi/2} \cos^x\theta d\theta, \tag{C10}$$

and $\theta_p = \tan^{-1}(k_p/k_1)$, representing the angle of integration where the spectral slope changes from a_1 to a_2. In (C8), the coefficient A_2 has been related to A_1 by the requirement that at $k = k_p$, the two expressions on the right-hand side of (C3) are identical, that is,

$$A_2 = A_1 k_p^{a_2-a_1} \cos^{p_1-p_2}\theta. \tag{C11}$$

If the directional distribution does not vary within the wavenumber range of integration, the cosine term in (C11) can be dropped. From numerical computation, it is found that the second term in (C8) contributes very little compared to the first term. Two examples for $a_1 = 4$ and $a_2 = 6$, corresponding to the results of the present dataset, are shown in Fig. C1 for $p_1 = p_2 = 0.5$ and $p_1 = p_2 = 2$. The coefficients $I_p(4)$ and $k_p^2 I_{p*}(6)$ versus k_1, which changes the integration limit, θ_p, in (C9) and (C10), are shown in Figs. C1a and C1b; the contribution from the second term is small, as noted earlier, except as k_1 approaches k_p. For all practical purposes, (C8) and (C5) can be expressed as

$$\chi(k_1) = \begin{cases} A_1 k_1^{1-a_1} I(a_1 + p_1 - 2), & k_1 < k_p \\ A_2 k_1^{1-a_2} I(a_2 + p_2 - 2), & k_1 > k_p. \end{cases} \tag{C12}$$

The ratio between (C8) and the first expression of (C12) is also plotted in Figs. C1a and C1b with the asterisk symbol. The calculated results indicate that the approximation (C12) is accurate to within 10% error compare to the full expression (C8). The function $I(x)$ is plotted in Fig. C1c. For the observed spectral function, $a_1 = 4$, $a_2 = 6$; p_1 and p_2 are unknown but probably in the neighborhood of 0.5 (Phillips 1985), therefore the proportionality con-

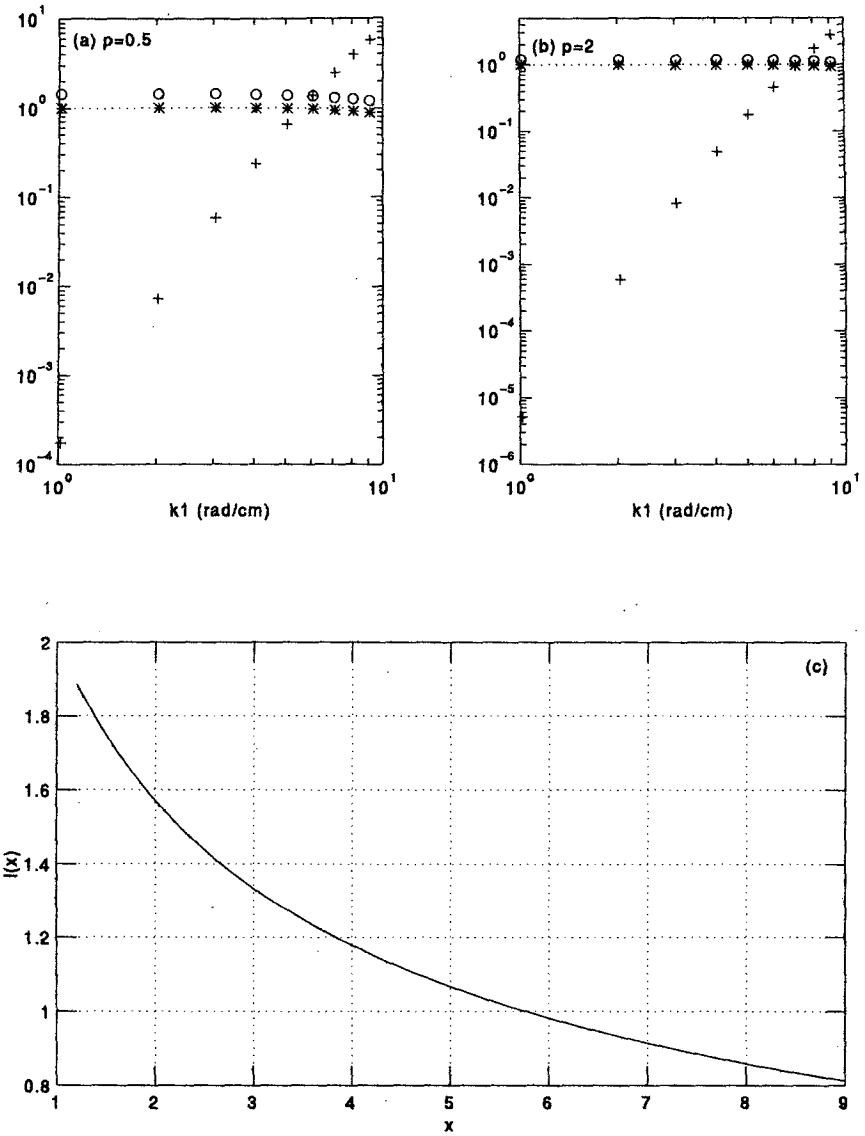

FIG. C1. (a) O: function $I_p(4)$ in (C8) and (C9); +: coefficient $k_p^2 I_{p*}(6)$ in (C8) and (C10), plotted against k_1; *: ratio of (C8) and the first expression of (C12); $p = 0.5$. The dashed line is 1, drawn for reference. (b) Same as (a) except for $p = 2$. (c) Function $I(x)$ of (C6) and (C12).

stant is close to 1. For example, $I(2) = 1.5708$, $I(4) = 1.1781$, and $I(6) = 0.9817$.

REFERENCES

Banner, M. L., 1990: Equilibrium spectra of wind waves. *J. Phys. Oceanogr.*, **20,** 966–984.

——, and O. M. Phillips, 1974: On the incipient breaking of small scale waves. *J. Fluid Mech.*, **65,** 647–656.

——, I. S. F. Jones, and J. C. Trinder, 1989: Wavenumber spectra of short gravity waves. *J. Fluid Mech.*, **198,** 321–344.

Cox, C. S., 1958: Measurements of slopes of high-frequency wind waves. *J. Mar. Res.*, **13,** 199–225.

——, and W. Munk, 1954: Statistics of the sea surface derived from sun glitter. *J. Mar. Res.*, **13,** 198–227.

Crombie, D. D., 1955: Doppler spectrum of sea echo at 13.56 Mc./s. *Nature*, **175,** 681–682.

Dobson, F., 1985: Comment on "Measurement of high-frequency waves using a wave follower" by S. Tang and O. H. Shemdin. *J. Geophys. Res.*, **90,** 9203–9204.

Donelan, M. A., and W. J. Pierson, 1987: Radar scattering and equilibrium ranges in wind-generated waves with application to scatterometry. *J. Geophys. Res.*, **92,** 4971–5029.

Hara, T., E. J. Bock, and D. Lyzenga, 1994: In situ measurements of capillary–gravity wave spectra using a scanning laser slope gauge and microwave radars. *J. Geophys. Res.*, **99,** 12 593–12 602.

Hughes, B. A., and H. L. Grant, 1978: The effect of internal waves on surface wind waves. Part 1: Experimental measurements. *J. Geophys. Res.*, **83,** 443–454.

——, and J. F. R. Gower, 1983: SAR imagery and surface truth comparisons of internal waves in Georgia Strait, British Columbia, Canada. *J. Geophys. Res.*, **88,** 1809–1824.

——, H. L. Grant, and R. W. Chappell, 1977: A fast response surface-wave slope meter and measured wind-wave moment. *Deep-Sea Res.*, **24,** 1211–1223.

Huhnerfuss, H., 1986: The molecular structure of the system water/monomolecular surface film and its influence on water wave damping. *Habilitationsschrift, Fachbereich Chemie,* University of Hamburg, 245 pp.

——, A. Gericke, W. Alpers, R. Theis, V. Wismann, and P. A. Lange, 1994: Classification of sea slicks by multifrequency radar techniques: New chemical insights and their geophysical implications. *J. Geophys. Res.*, **99,** 9835–9845.

Hwang, P. A., 1992: Optical measurements of short wave modulation by surface currents. *Optics of the Air–Sea Interface: Theory and Measurement,* Vol. 1749, Int. Soc. Opt. Eng., 216–221.

——, and O. H. Shemdin, 1988: The dependence of sea surface slope on atmospheric stability and swell conditions. *J. Geophys. Res.*, **93,** 13 903–13 912.

——, and ——, 1990: Modulation of short surface waves by surface currents—a numerical solution. *J. Geophys. Res.*, **95,** 16 311–16 318.

——, D. B. Trizna, and J. Wu, 1993: Spatial measurements of short wind waves using a scanning slope sensor. *Dyn. Atmos. Oceans,* **20,** 1–23.

Jahne, B., and K. S. Riemer, 1990: Two-dimensional wavenumber spectra of small-scale water surface waves. *J. Geophys. Res.*, **95,** 11 531–11 546.

Kinsman, B., 1965: *Wind Waves, Their Generation and Propagation on the Ocean Surface.* Prentice-Hall, 676 pp.

Lamb, H., 1945: *Hydrodynamics.* 6th ed. Dover, 738 pp.

Lawner, R. T., and R. K. Moore, 1984: Short gravity and capillary wave spectra from tower-based radar. *IEEE J. Oceanic Eng.,* **OE-9,** 317–324.

Lee, P. H. Y., J. D. Barter, K. L. Beach, C. L. Hindman, B. M. Lake, H. Rungaldier, J. C. Schatzman, J. C. Shelton, R. N. Wagner, A. B. Williams, R. Yee, and H. C. Yuen, 1992: Recent advances in ocean surface characterization by a scanning laser slope gauge. *Optics of the Air–Sea Interface: Theory and Measurement,* Vol. 1749, Int. Soc. Opt. Eng., 234–244.

Lighthill, J., 1979: *Waves in Fluids.* Cambridge University Press, 504 pp.

Liu, W. T., K. B. Katsaros, and J. A. Businger, 1979: Bulk parameterization of air–sea exchanges of heat and water vapor including the molecular constraints at the interface. *J. Atmos. Sci.*, **36,** 1722–1735.

Longuet-Higgins, M. S., 1963: The generation of capillary gravity waves by steep gravity waves. *J. Fluid Mech.*, **16,** 138–159.

——, 1992: Capillary rollers and bores. *J. Fluid Mech.*, **240,** 659–679.

Martinsen, R. J., and E. J. Bock, 1992: Optical measurements of ripples using a scanning laser slope gauge. Part I: Instrumentation and preliminary results. *Optics of the Air-Sea Interface: Theory and Measurement,* Vol. 1749, Int. Soc. Opt. Eng., 258–271.

Mitsuyasu, H., 1977: Measurement of the high-frequency spectrum of ocean surface waves. *J. Phys. Oceanogr.*, **7,** 882–891.

Palm, C. S., R. C. Anderson, and A. M. Reece, 1977: Laser probe for measuring 2-D wave slope spectra of ocean capillary waves. *Appl. Opt.*, **16,** 1074–1081.

Perlin, M., H. Lin, and C.-L. Ting, 1993: On parasitic capillary waves generated by steep gravity waves: An experimental investigation with spatial and temporal measurements. *J. Fluid Mech.*, **255,** 597–620.

Phillips, O. M., 1977: *The Dynamics of the Upper Ocean.* 2d ed. Cambridge University Press, 336 pp.

——, 1985: Spectral and statistical properties of the equilibrium range in wind-generated gravity waves. *J. Fluid Mech.*, **156,** 505–531.

——, 1988: Radar returns from the sea surface—Bragg scattering and breaking waves. *J. Phys. Oceanogr.*, **18,** 1065–1074.

——, and M. L. Banner, 1974: Wave breaking in the presence of wind drift and swell. *J. Fluid Mech.*, **107,** 625–640.

Schule, J. J., L. S. Simpson, and P. S. DeLeonibus, 1971: A study of fetch limited wave spectra with an airborne laser. *J. Geophys. Res.*, **76,** 4160–4171.

Shemdin, O. H., and P. A. Hwang, 1988: Comparison of measured and predicted sea surface spectra of short waves. *J. Geophys. Res.*, **93,** 13 883–13 890.

Sletten, M., D. B. Trizna, and P. A. Hwang, 1994: Ambient light calibration of a scanning slope sensor. Naval Research Laboratory Memo. Rep. No. 7743.

Tang, S., and O. H. Shemdin, 1983: Measurements of high frequency waves using a wave follower. *J. Geophys. Res.*, **88,** 9832–9840.

Thompson, D. R., 1988: Calculation of radar backscatter modulation from internal waves. *J. Geophys. Res.*, **93,** 12 371–12 380.

——, and R. F. Gasparovic, 1986: Intensity modulation in SAR images of internal waves. *Nature,* **320,** 345–348.

Trizna, D. B., J. P. Hansen, P. A. Hwang, and J. Wu, 1993: Ultra-wideband radar studies of steep crested waves with scanning laser measurements of wave slope profiles. *Dyn. Atmos. Oceans,* **20,** 33–53.

Wetzel, L. B., 1993: A time domain model for sea scatter. *Radio Sci.*, **28,** 139–150.

Wright, J. W., 1966: Backscattering from capillary waves with application to sea clutter. *IEEE Trans. Antennas Propag.*, **AP-14,** 749–754.

——, 1968: A new model for sea clutter. *IEEE Trans. Antennas Propag.*, **AP-16,** 217–223.